GEOMETRIC TRIANGULATION OF IMAGING OBSERVATIONS TO TRACK CORONAL MASS EJECTIONS CONTINUOUSLY OUT TO 1 AU

2010 ApJ 710 L82

(http://iopscience.iop.org/2041-8205/710/1/L82)

The Astrophysical Journal Letters, 710:L82–L87, 2010 February 10 doi:10.1088/2041-8205/710/1/L82

GEOMETRIC TRIANGULATION OF IMAGING OBSERVATIONS TO TRACK CORONAL MASS EJECTIONS CONTINUOUSLY OUT TO 1 AU

Ying Liu[1], Jackie A. Davies[2], Janet G. Luhmann[1], Angelos Vourlidas[3], Stuart D. Bale[1], and Robert P. Lin[1,4]
[1] Space Sciences Laboratory, University of California, Berkeley, CA 94720, USA; liuxying@ssl.berkeley.edu
[2] Space Science and Technology Department, Rutherford Appleton Laboratory, Didcot, UK
[3] Space Science Division, Naval Research Laboratory, Washington, DC 20375, USA
[4] School of Space Research, Kyung Hee University, Yongin, Gyeonggi 446-701, Republic of Korea
Received 2009 September 22; accepted 2010 January 8; published 2010 January 22

ABSTRACT

We describe a geometric triangulation technique, based on time–elongation maps constructed from imaging observations, to track coronal mass ejections (CMEs) continuously in the heliosphere and predict their impact on the Earth. Taking advantage of stereoscopic imaging observations from the Solar Terrestrial Relations Observatory, this technique can determine the propagation direction and radial distance of CMEs from their birth in the corona all the way to 1 AU. The efficacy of the method is demonstrated by its application to the 2008 December 12 CME, which manifests as a magnetic cloud (MC) from in situ measurements at the Earth. The predicted arrival time and radial velocity at the Earth are well confirmed by the in situ observations around the MC. Our method reveals non-radial motions and velocity changes of the CME over large distances in the heliosphere. It also associates the flux-rope structure measured in situ with the dark cavity of the CME in imaging observations. Implementation of the technique, which is expected to be a routine possibility in the future, may indicate a substantial advance in CME studies as well as space weather forecasting.

Key words: solar–terrestrial relations – solar wind – Sun: coronal mass ejections (CMEs)

Online-only material: animations

1. INTRODUCTION

Coronal mass ejections (CMEs) are large-scale expulsions of plasma and magnetic field from the solar atmosphere and have been recognized as primary drivers of interplanetary disturbances. Tracking CMEs continuously from the Sun to the Earth is crucial for at least three aspects: a practical capability in space weather forecasting which has important consequences for life and technology on the Earth and in space; accurate measurements of CME kinematics over an extensive region of the heliosphere that are needed to constrain global magnetohydrodynamic (MHD) simulations of CME evolution; determination of CME properties from imaging observations that can be properly compared with in situ data.

CMEs and shocks have been tracked continuously in the heliosphere using type II radio emissions (e.g., Reiner et al. 2007; Liu et al. 2008) and MHD propagation of observed solar wind disturbances (e.g., Wang et al. 2001; Richardson et al. 2005, 2006; Liu et al. 2006b, 2008). The frequency drift of type II bursts can be used to characterize shock propagation but relies on a density model to convert frequencies to heliocentric distances; in situ measurements of shock parameters at 1 AU are also needed to constrain the overall height-time profile due to ambiguities in the frequency drift. MHD propagation of the solar wind, connecting in situ measurements at different distances, has been performed only for CME/shock propagation beyond 1 AU as confined by availability of in situ measurements close to the Sun. None of these techniques can determine the propagation direction.

Accurate determination of the propagation direction is feasible with multiple views of the Sun–Earth space from the Solar Terrestrial Relations Observatory (STEREO; Kaiser et al. 2008). Geometric triangulation techniques using the stereoscopic imaging observations have been developed to determine the CME propagation direction and radial distance (e.g., Pizzo & Biesecker 2004; Howard & Tappin 2008; Maloney et al. 2009). All of these methods require the identification and tracking of the same feature in image pairs from the two spacecraft. This is not possible at large distances where CME signals become very faint and diffusive, especially in the field of view (FOV) of the heliospheric imagers (HI1 and HI2). Construction of time–elongation maps from imaging observations, which can sense weak signals, has been extended to HI1 and HI2 data (e.g., Sheeley et al. 2008; Rouillard et al. 2008; Davies et al. 2009). A kinematic model with various assumptions on the acceleration or velocity of the transient activity is used to fit the tracks in the time–elongation plot (Sheeley et al. 1999); in order to reduce the number of free parameters, CMEs are assumed to move radially at a constant velocity in the FOV of HI1 and HI2 (e.g., Sheeley et al. 2008; Rouillard et al. 2008; Davies et al. 2009). This is a least-squares fit and deals with the minimization of a chi-square statistic; without a priori knowledge, it is difficult to check whether the solutions have converged to a global minimum or just a local one. Therefore, CME kinematics (especially the propagation direction) cannot be determined unambiguously with the track fitting technique. In addition, the model fit does not take advantage of geometric triangulation even though the fit can be performed independently for the two spacecraft. The full promise of the twin stereo views has yet to be realized.

In this Letter, we incorporate geometric triangulation in the time–elongation map analysis using imaging observations from STEREO. The advantage of this method is that, first, it is based on time–elongation plots, so geometric triangulation can be applied to weak features in HI1 and HI2 for the first time; second, it relies on fewer assumptions than the single track fitting technique, so the solution would be more accurate; third, it can determine the propagation direction and true distance of CME features (or other white-light features) from the Sun all the way to 1 AU. This technique is relatively robust and

may indicate an important advance for CME studies and space weather forecasting.

2. INSTRUMENTS AND METHODOLOGY

Figure 1 shows the configuration of the two spacecraft with respect to the Sun. We focus on CME propagation in the ecliptic plane, since from the perspective of space weather prediction it is important to know whether/when a CME will impact the Earth. STEREO A is moving faster and slightly closer to the Sun than the Earth, while STEREO B is a little further and trailing the Earth; the angular separation between each spacecraft and the Earth increases by about 22.°5 per year. Each spacecraft carries an identical imaging suite, the Sun Earth Connection Coronal and Heliospheric Investigation (SECCHI; Howard et al. 2008), which consists of an EUV imager (EUVI), two coronagraphs (COR1 and COR2), and two heliospheric imagers (HI1 and HI2). COR1 and COR2 have an FOV of 0.°4–1° and 0.°7–4° around the Sun, respectively. HI1 has a 20° square FOV centered at 14° elongation from the center of the Sun while HI2 has a 70° FOV centered at 53.°7 from the Sun center. Combined together these cameras can image a CME from its nascent stage in the corona all the way to the Earth (see the accompanying animations online; also see Liu et al. 2009).

This new instrumentation, especially the HIs, seems so useful that it will be routinely used in the future. However, geometric triangulation of HI1 and HI2 data taking advantage of the two vantage points off the Sun–Earth line has not been implemented since CME signals in their FOVs are often weak and diffusive. Here, we develop a geometric triangulation technique, applicable to all these cameras, to determine the radial distance and propagation direction of CMEs. As shown in Figure 1, a white-light feature would be seen by the two spacecraft as long as it moves along a direction between them. The elongation angle of the feature (the angle of the feature with respect to the Sun-spacecraft line), denoted as α_A and α_B for STEREO A and B respectively, can be measured from imaging observations transformed into a Sun-centered coordinate system. This simple geometry gives

$$\frac{r\sin(\alpha_A+\beta_A)}{\sin\alpha_A}=d_A, \tag{1}$$

$$\frac{r\sin(\alpha_B+\beta_B)}{\sin\alpha_B}=d_B, \tag{2}$$

$$\beta_A+\beta_B=\gamma, \tag{3}$$

where r is the radial distance of the feature from the Sun, β_A and β_B are the propagation angles of the feature relative to the Sun-spacecraft line, d_A and d_B are the distances of the spacecraft from the Sun (known), and γ is the longitudinal separation between the two spacecraft (also known). Once the elongation angles (α_A and α_B) are measured from imaging observations, the above equations can be solved for r, β_A, and β_B, a unique set of solutions (compared with model fit). For $d_A = d_B$, these equations can be reduced to

$$\tan\beta_A=\frac{\sin\alpha_A\sin(\alpha_B+\gamma)-\sin\alpha_A\sin\alpha_B}{\sin\alpha_A\cos(\alpha_B+\gamma)+\cos\alpha_A\sin\alpha_B}, \tag{4}$$

which is generally true for STEREO A and B and allows a quick estimate of the propagation direction.

The elongation angles can be obtained from time–elongation plots produced by stacking the running difference intensities

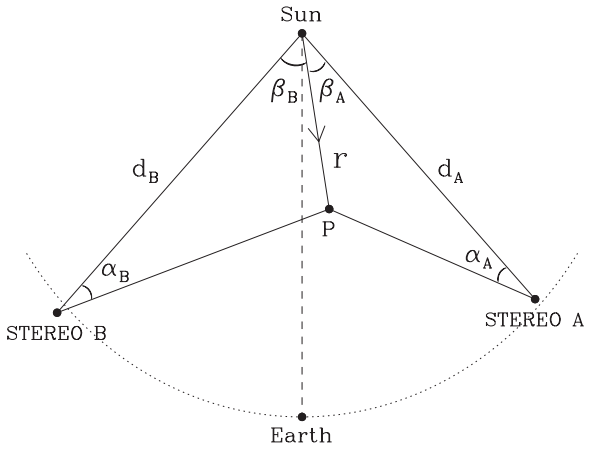

Figure 1. Diagram for the geometric triangulation in the ecliptic plane. The dotted line indicates the orbit of the Earth while the dashed line represents the Sun–Earth line. A white-light feature, propagating along the direction shown by the arrow, is denoted by the point P.

along the ecliptic plane. Even weak signals are discernible in these maps, so transient activity can be revealed over an extensive region of the heliosphere. CME features usually appear as tracks extending to large elongation angles in the maps. Previous studies use only Equation (1) or (2) to fit the tracks assuming a kinematic model with a constant propagation direction (e.g., Sheeley et al. 1999, 2008; Rouillard et al. 2008; Davies et al. 2009; Davis et al. 2009).

Our only assumption is that the same feature can be tracked in both the time–elongation maps from the two spacecraft. This is likely true if the tracks between the maps have a good timing (see details below). COR1 and COR2 have a cadence of 5 minutes and 15 minutes, respectively; tracking of the same feature from the timing is good to these timescales. However, the imaging observations provide integrated line-of-sight information through a three-dimensional structure. Projection and Thomson-scattering effects may affect the tracks in the time–elongation maps in ways that are difficult to assess quantitatively without detailed modeling of the coronal brightness (Vourlidas & Howard 2006; Lugaz et al. 2008, 2009). Such effects are minimized for features propagating symmetrically relative to the two spacecraft (i.e., along the Sun–Earth line). The uncertainties brought about by these effects will be addressed by global MHD simulations in an ongoing work.

3. APPLICATION

To prove the efficacy of the method, we apply it to the 2008 December 12 CME. Figure 2 shows two synoptic views of the CME from STEREO A and B. During the time of the CME, $\gamma \simeq 86.°3$, $d_A \simeq 0.97$ AU, and $d_B \simeq 1.04$ AU; STEREO A and B are generally within 5° of the ecliptic plane. The latitudinal separation between the two spacecraft is ignored in our triangulation analysis for simplicity. A panoramic view of the CME evolution from the low corona to the Earth is also provided in the online journal as animations made of composite images from the complete imaging system. The CME is induced by a prominence eruption in the northern hemisphere, which started between 03:00 UT and 04:00 UT on December 12. The prominence material (visible in EUVI at 304 Å) is well aligned with the CME core. The CME slowly rotates and expands toward the ecliptic plane, and seems fully developed in COR2. Running difference images are used for HI1 and HI2 to remove

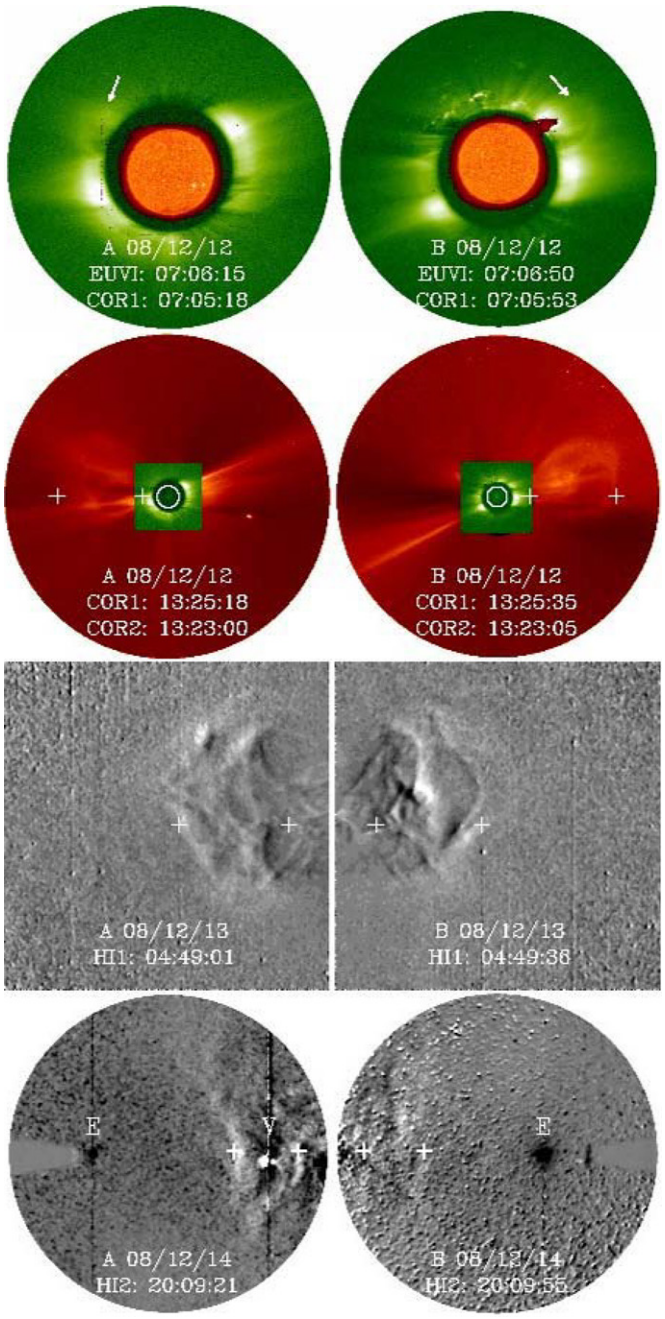

Figure 2. CME evolution observed by STEREO A (left) and B (right) near simultaneously. From top to bottom, the panels display the composite images of EUVI at 304 Å and COR1 showing the nascent CME (indicated by the arrow), combined COR1 and COR2 images of the fully developed CME, and running difference images from HI1 and HI2 when the CME is far away from the Sun. The crosses mark the locations of the two features obtained from Figure 3. The positions of the Earth and Venus are labeled as E and V.

(Animations of this figure are available in the online journal.)

the F corona (produced by dust scattering of the white light) and stellar background. The Earth is visible in HI2 from both STEREO A and B, while Venus is seen only from STEREO A; their brightness saturates the detector, resulting in a vertical line in the image. Oscillation of stars is also visible in HI2 from STEREO B, probably due to a slight shaking of the camera. The basic structure of the CME remains organized out to the FOV of HI1 (close to the Sunward edge), but only wave-like structures are seen in HI2. Apparently the weak diffusive signal is difficult to track using traditional techniques.

The time–elongation maps shown in Figure 3 are produced by stacking running difference intensities of COR2, HI1, and HI2 within a slit of 64 pixels around the ecliptic plane. In the FOVs of HI1 and HI2, the coronal intensity is dominated by the F corona and stellar background. The contribution of the F corona is minimized by subtracting a long-term background from each image. Adjacent images are aligned prior to the running differencing to remove stars from the FOV. Both the image alignment and determination of elongation angles require precise pointing information of the HI cameras, so we use the level 1 data (available at http://www.ukssdc.rl.ac.uk/solar/stereo/data.html) that have been corrected for flat field, shutterless readout, and instrument offsets from the spacecraft pointing. We apply a median filter to these difference images to reduce the residual stellar effects. A radial strip with a width of 64 pixels around the ecliptic plane is extracted from each difference image, and a resistant mean is taken over the 64 pixels to represent the intensity at corresponding elongation angles. These resistant means are then stacked as a function of time and elongation, and the resulting map is scaled to enhance transient signals.

In Figure 3, two features coincident with the CME can be identified up to 50° elongation for both STEREO A and B. For comparison, the Earth is at an elongation angle of 70° for STEREO A and 64° for STEREO B. The temporal coincidence of each track between the two maps indicates that we are tracking the same feature. Intermittent ones between the two tracks, probably associated with the CME core, are also seen but later disappear presumably due to the expansion of the CME (see Figure 5). Note that the elongation angles are plotted in a logarithmic scale to expand COR2 data; tracks are not J-like as in traditional linear–linear plots. Elongation angles are extracted along the trailing edge of these two tracks (with the sharpest contrast); interpolation is then performed to get elongation angles at the same time tags for STEREO A and B as required by the triangulation analysis. The uncertainty in the measurements of elongation angles is estimated to be about 10 pixels, which is roughly 0.°02, 0.°2, and 0.°7 for COR2, HI1, and HI2, respectively. We input the values of the elongation angles to Equations (1)–(4) to calculate the propagation direction and radial distance. Time–elongation maps from COR1 images are also examined but not included here, given its small FOV and the fact that the CME is largely above the ecliptic plane through COR1.

The resulting CME kinematics are displayed in Figure 4. The propagation direction (β_A or β_B) is converted to an angle with respect to the Sun–Earth line. If the angle is positive (negative), the CME feature would be propagating west (east) of the Sun–Earth line in the ecliptic plane. The propagation direction (for both features 1 and 2) shows a variation with distance but is generally within 5° of the Sun–Earth line. These features can be continuously tracked up to 150 solar radii or 0.7 AU (without projection). Radial velocities are derived from the distance using a numerical differentiation with three-point Lagrangian interpolation. The radial velocity also shows a variation with distance: it first increases rapidly and then decreases (clearer for feature 1 which is the CME leading edge). The radial velocity is about 363 ± 43 km s^{-1} for feature 1 and 326 ± 51 km s^{-1} for feature 2 close to the Earth, estimated by averaging data points after December 14. Note that, different from previous studies, our method is unique since it can determine CME kinematics (both propagation direction and radial velocity) as a function of distance from the Sun all the way to 1 AU; the CME kinematics determined this way provide an

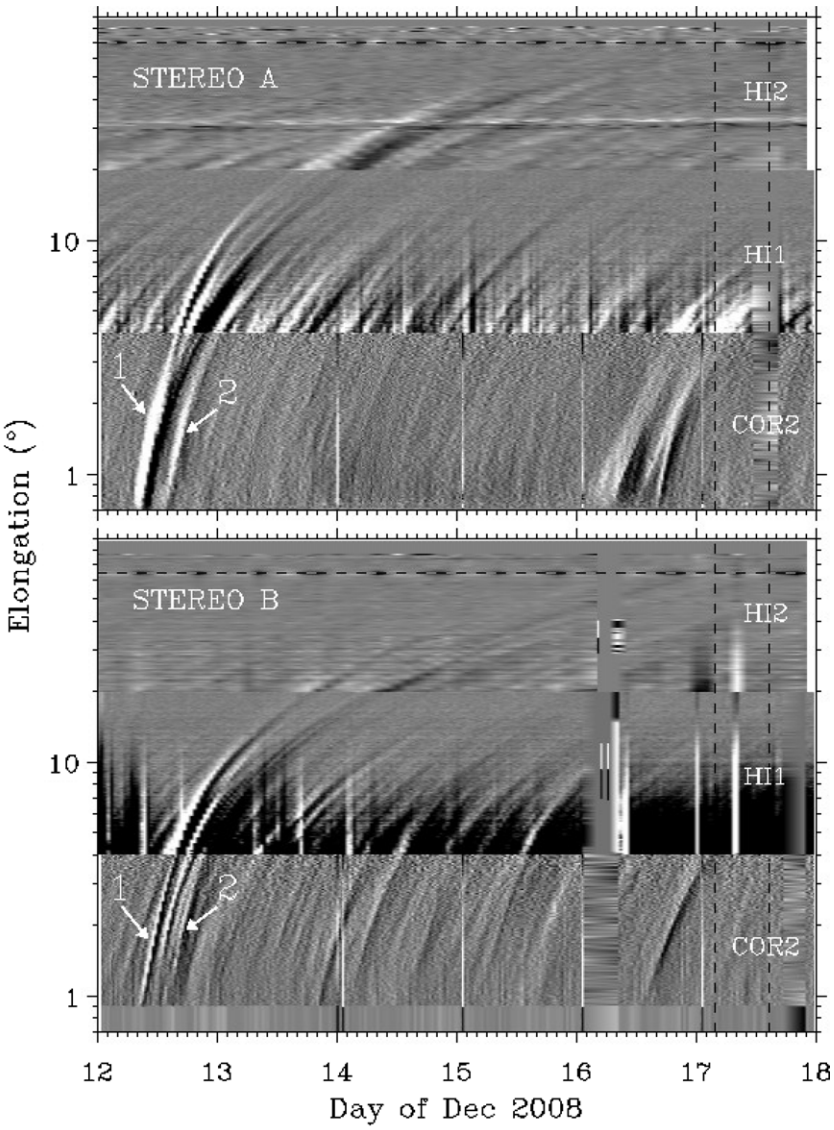

Figure 3. Time-elongation maps constructed from running difference images of COR2, HI1, and HI2 along the ecliptic plane for STEREO A (upper) and B (lower). The arrows indicate two tracks associated with the CME. The vertical dashed lines show the MC interval observed at WIND, and the horizontal dashed line marks the elongation angle of the Earth.

unprecedented opportunity to constrain global MHD models of CME evolution.

We test these results using in situ measurements. Figure 5 shows a magnetic cloud (MC) identified from WIND data based on the strong magnetic field and smooth rotation of the field. A similar field and velocity structure is also observed at the *Advanced Composition Explorer* (*ACE*), but *ACE* does not have valid measurements of proton density and temperature due to the low solar wind speeds during this time interval (R. M. Skoug 2009, private communication). The MC radial width (average speed times the duration) is about 0.1 AU, relatively small compared with the average level 0.2–0.3 AU at 1 AU (e.g., Liu et al. 2005, 2006a). It is remarkable that even such a small event can be tracked to those large distances. The MC density is lower than that of the ambient solar wind, presumably owing to the expansion as shown by the declining speed profile across the MC. The MC has a well-organized magnetic field structure; our reconstruction with the Grad–Shafranov method gives a left-handed flux-rope configuration. This is surprising given the imprint of a rather diffusive morphology in HI2 images. The predicted arrival times of features 1 and 2, obtained with a second-order polynomial fit of the radial distance shown in Figure 4, bracket the MC and are coincident with density-enhanced structures around the MC. It is interesting that these high-density structures, which appear to be part of the CME in imaging observations, are actually not contained in the flux rope. This finding supports the view that the flux rope corresponds to the dark cavity in the classic three-part structure of CMEs (front, cavity, and core). The arrival time prediction is good to within a few hours. Note that we are not tracking the flux rope but density-enhanced regions before and after the MC, and the CME front has swept up and merged with the ambient solar wind during its propagation in the heliosphere. The predicted radial velocities at 1 AU, an average over the data points after December 14 in Figure 4, are also well confirmed by in situ measurements.

The good agreement between the geometric triangulation analysis and in situ data demonstrates a technique that can predict CME impact well in advance; remote sensing observations can also be properly connected with in situ measurements with

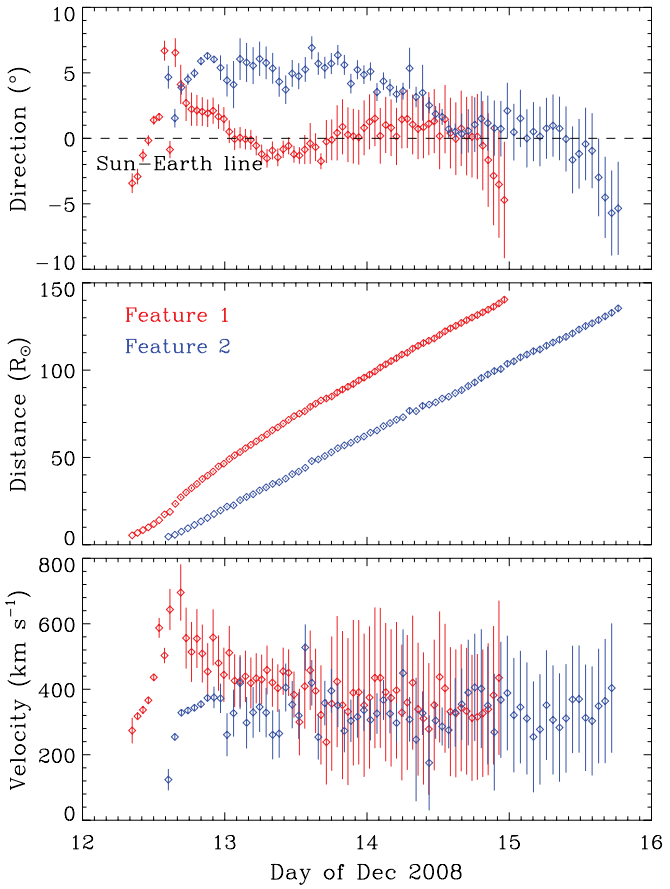

Figure 4. Propagation direction, radial distance, and velocity of features 1 (red) and 2 (blue) derived from the geometric triangulation analysis. The dashed line indicates the Sun–Earth line. Error bars represent uncertainties mathematically derived from the measurements of elongation angles. Note that the velocities are calculated from adjacent distances and often have misleading error bars.

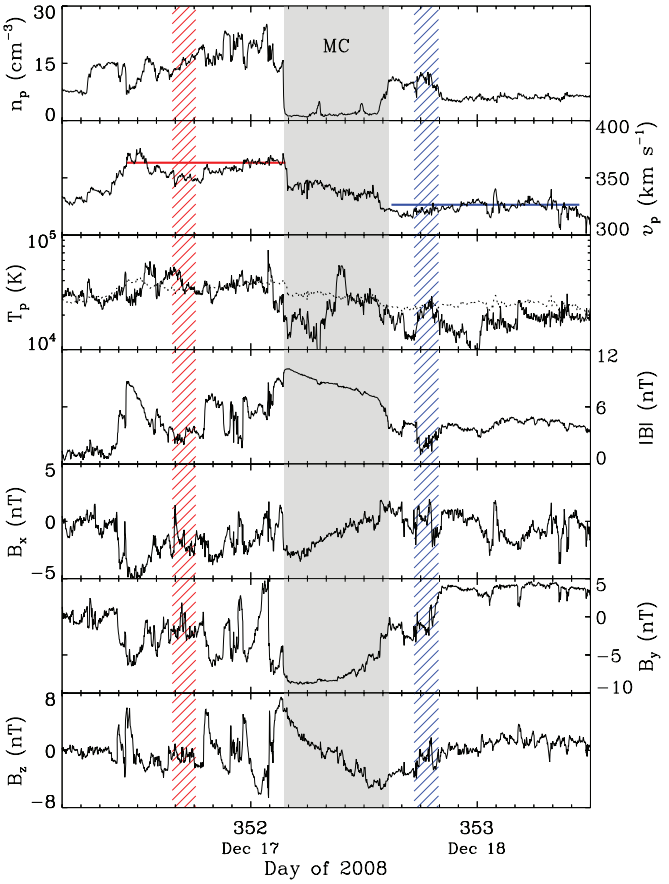

Figure 5. Solar wind plasma and magnetic field parameters across the MC observed at WIND. From top to bottom, the panels show the proton density, bulk speed, proton temperature, and magnetic field strength and components, respectively. The shaded region indicates the MC interval, and the hatched area shows the predicted arrival times (with uncertainties) of features 1 (red) and 2 (blue). The horizontal lines mark the corresponding predicted velocities at 1 AU. The dotted line denotes the expected proton temperature from the observed speed.

the aid of the method. Various attempts have also been made to predict CME arrival times at the Earth with an accuracy ranging from 2 hr to 11 hr (e.g., Zhao et al. 2002; Michalek et al. 2004; Howard et al. 2006). The present method is expected to give a more accurate prediction since it can track CMEs from the Sun continuously to 1 AU. A statistical study, however, is needed before we affirm the effectiveness of the technique.

Davis et al. (2009) studied the same event based on a single spacecraft analysis (HI data only). They assumed a kinematic model with a constant velocity and propagation direction, which has the least free parameters. Their results are roughly similar to ours, except that they obtain a radial velocity larger than observed and a larger uncertainty in the propagation direction (see their Table 1). It is not surprising that, given such a small CME, their assumptions of constant velocity and propagation direction in the FOV of the HIs are more or less verified by our results. These assumptions are usually not true for CME propagation close to the Sun (see Figure 4). Fast CMEs would have a strong interaction with the heliosphere, and thus their velocities vary with distance even far away from the Sun (e.g., Liu et al. 2008). The single track fitting approach, however, still remains useful especially when data are only available from one spacecraft.

4. SUMMARY

We have presented a geometric triangulation technique to track CMEs from the Sun all the way to 1 AU, based on stereoscopic imaging observations of STEREO. This new method enables geometric triangulation for HI1 and HI2 data, relaxes various assumptions needed in a model fit (e.g., Sheeley et al. 1999, 2008; Rouillard et al. 2008; Davies et al. 2009), and can accurately determine CME kinematics (both propagation direction and radial distance) continuously in the heliosphere. A good agreement between the geometric triangulation analysis and in situ measurements is obtained when we apply the method to the 2008 December 12 CME. Velocity changes and non-radial motions of the CME are also revealed by the tracking technique; this propagation history over a large distance is crucial to probe CME interaction with the heliosphere. This method enables a better connection between imaging and in situ observations. It fulfills a major objective of the STEREO mission and also heralds a new era when CMEs can be tracked over a far more extensive region of the heliosphere than previously possible with coronagraph observations.

The research was supported by the STEREO project under grant NAS5-03131. SECCHI was developed by a consortium of NRL, LMSAL and GSFC (US), RAL and the University of Birmingham (UK), MPI (Germany), CSL (Belgium), and IOTA and IAS (France). We acknowledge the use of WIND data. R. Lin has been supported in part by the WCU grant (No. R31-10016) funded by KMEST.

REFERENCES

Davies, J. A., et al. 2009, Geophys. Res. Lett., 36, L02102
Davis, C. J., Davies, J. A., Lockwood, M., Rouillard, A. P., Eyles, C. J., & Harrison, R. A. 2009, Geophys. Res. Lett., 36, L08102
Howard, R. A., et al. 2008, Space Sci. Rev., 136, 67
Howard, T. A., & Tappin, S. J. 2008, Sol. Phys., 252, 373
Howard, T. A., Webb, D. F., Tappin, S. J., Mizuno, D. R., & Johnston, J. C. 2006, J. Geophys. Res., 111, A04105
Kaiser, M. L., Kucera, T. A., Davila, J. M., St. Cyr, O. C., Guhathakurta, M., & Christian, E. 2008, Space Sci. Rev., 136, 5
Liu, Y., Luhmann, J. G., Bale, S. D., & Lin, R. P. 2009, ApJ, 691, L151
Liu, Y., Richardson, J. D., & Belcher, J. W. 2005, Planet. Space Sci., 53, 3
Liu, Y., Richardson, J. D., Belcher, J. W., Kasper, J. C., & Elliott, H. A. 2006a, J. Geophys. Res., 111, A01102
Liu, Y., Richardson, J. D., Belcher, J. W., Wang, C., Hu, Q., & Kasper, J. C. 2006b, J. Geophys. Res., 111, A12S03
Liu, Y., et al. 2008, ApJ, 689, 563
Lugaz, N., Vourlidas, A., & Roussev, I. I. 2009, Ann. Geophys., 27, 3479
Lugaz, N., Vourlidas, A., Roussev, I. I., Jacobs, C., Manchester, W. B., IV, & Cohen, O. 2008, ApJ, 684, L111
Maloney, S. A., Gallagher, P. T., & McAteer, R. T. J. 2009, Sol. Phys., 256, 149
Michalek, G., Gopalswamy, N., Lara, A., & Manoharan, P. K. 2004, A&A, 423, 729
Pizzo, V. J., & Biesecker, D. A. 2004, Geophys. Res. Lett., 31, L21802
Reiner, M. J., Kaiser, M. L., & Bougeret, J.-L. 2007, ApJ, 663, 1369
Richardson, J. D., Wang, C., Kasper, J. C., & Liu, Y. 2005, Geophys. Res. Lett., 32, L03S03
Richardson, J. D., et al. 2006, Geophys. Res. Lett., 33, L23107
Rouillard, A. P., et al. 2008, Geophys. Res. Lett., 35, L10110
Sheeley, N. R., Walters, J. H., Wang, Y.-M., & Howard, R. A. 1999, J. Geophys. Res., 104, 24739
Sheeley, N. R., et al. 2008, ApJ, 675, 853
Vourlidas, A., & Howard, R. A. 2006, ApJ, 642, 1216
Wang, C., Richardson, J. D., & Paularena, K. I. 2001, J. Geophys. Res., 106, 13007
Zhao, X. P., Plunkett, S. P., & Liu, W. 2002, J. Geophys. Res., 107, 1223